Supporting Information

Robust Ultra-Long Lead Halide Perovskite Microwire Lasers

Shanshan Yan,[†,#] Kaiyang Wang,[†,#] Guichuan Xing,[†] Jincheng Xu,[†] Shichen Su,[‡,§] Zikang Tang,[†] Shuangpeng Wang[,†] and Kar Wei Ng[*,†]*

[†]Joint Key Laboratory of the Ministry of Education, Institute of Applied Physics and Materials Engineering, University of Macau, Avenida da Universidade, Taipa 999078, Macau, China

[‡]Institute of Semiconductor Science and Technology, South China Normal University, Guangzhou 510631, China

[§]SCNU Qingyuan Institute of Science and Technology Innovation Co., Ltd., Qingyuan 511517, China

[*]Corresponding Authors

E-mail: spwang@um.edu.mo (S. W.),

E-mail: billyng@um.edu.mo (K. N.).

[#]These authors contributed equally to this work.

Figure S1 shows the $PbBr_2$ microwires synthesized with isopropanol as antisolvent. The SEM images illustrate that the selected 16 microwires possess relatively uniform size. Due to the relatively large polarity of IPA, the stacking along the axial direction will increase over time. As a result, the length of the obtained $PbBr_2$ microwires is relatively small within tens of microns.

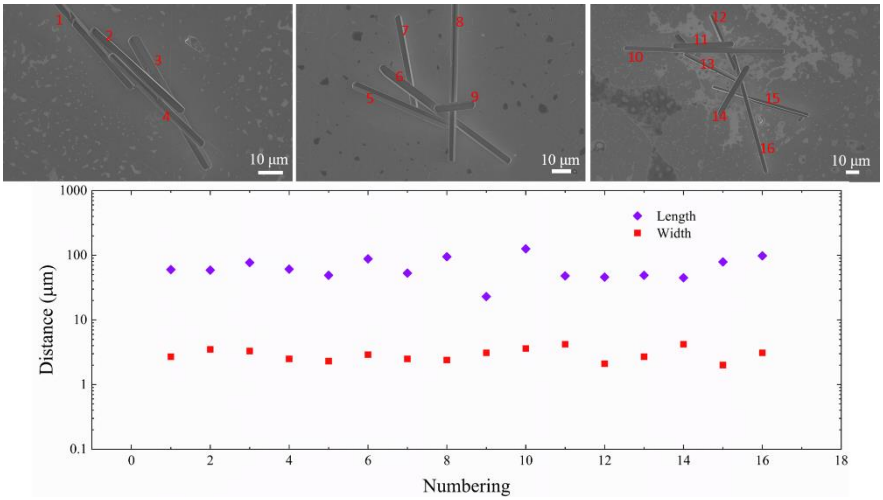

Figure S1. The uniform $PbBr_2$ microwires synthesized with IPA as antisolvent, with length ranges from 23 to 126 μm and width from 2.0 to 4.2 μm.

Figure S2 shows the $PbBr_2$ microwires synthesized with acetone as antisolvent. Since the polarity of acetone is lower than that of isopropanol, the acetone vapor will facilitate the growth of $PbBr_2$ along the axial direction and crystallized to form longer microwires. As a result, the length of the obtained $PbBr_2$ microwires is relatively large ranges within hundreds of microns. And the width of the as-prepared $PbBr_2$ microwires with the two different antisolvent method was nearly the same (average value ~3 μm).

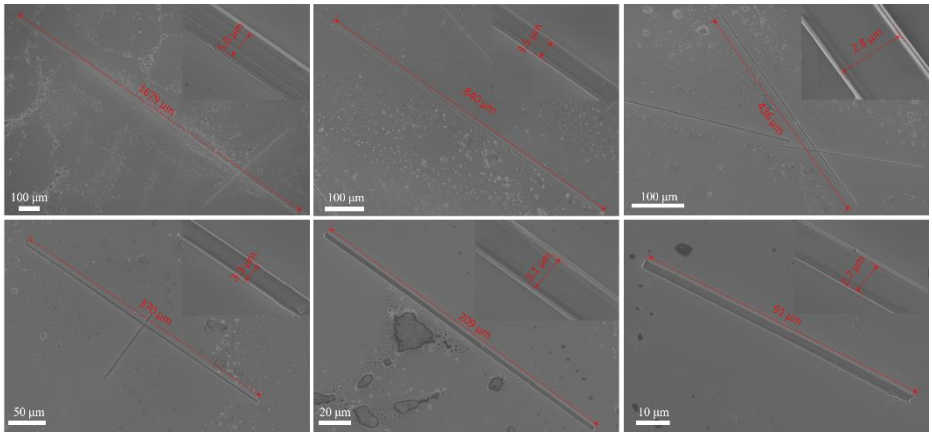

Figure S2. The $PbBr_2$ microwires with high aspect ratio synthesized with acetone as antisolvent, with length ranges from 91 to 1679 μm and width from 2.7 to 5.0 μm.

Figure S3 shows the rectangle region quantitative elemental analysis of the $PbBr_2$ microwire, and the ratio of Br/Pb is about 2.09, which is consistent with the stoichiometric ratio of lead bromide.

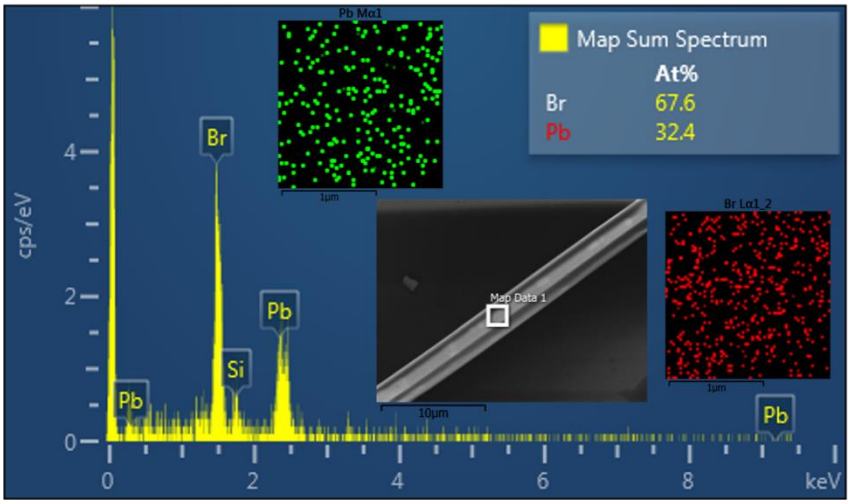

Figure S3. Representative EDX spectrum from single $PbBr_2$ microwire and quantitative elemental analysis yields an average Br/Pb ratio of 2.09**.**

Figure S4 shows the EDX mapping of the $MAPbBr_3$ microwires, and the C, N, Pb, Br elements are evenly distributed over the mapping area. In addition, the quantitative elemental analysis also indicates the Br/Pb ratio is 2.89/1.11, which agrees well with the stoichiometric ratio of methylamine lead bromide. As a result, the element mapping and stoichiometric ratio prove the completeness of the transformation process.

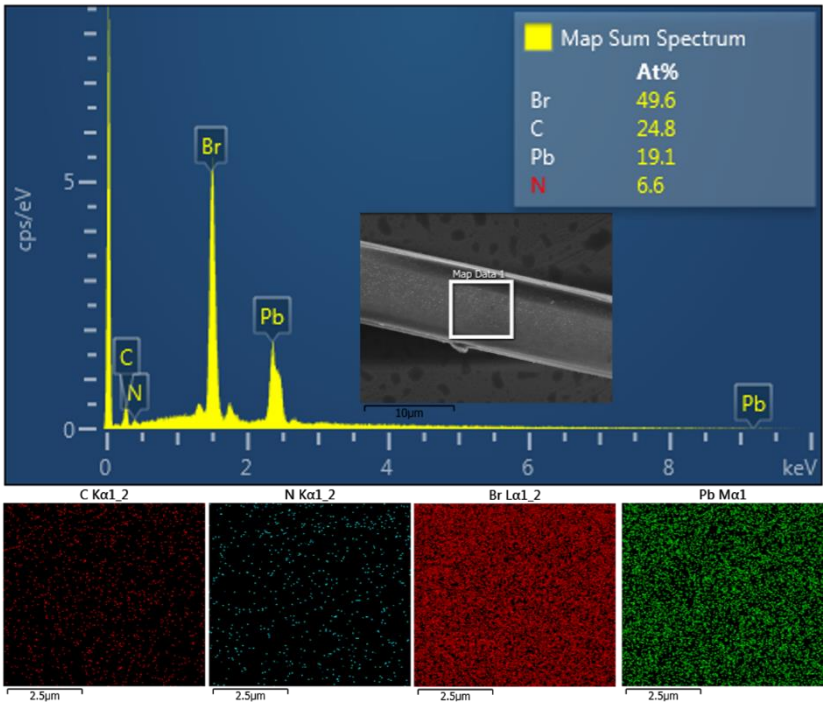

Figure S4. The mapping images of C, N, Pb, Br elements from the rectangle area on the surface of $MAPbBr_3$ microwire, and the average Br/Pb ratio is 2.89/1.11.

Figure S5 shows the Raman spectra of $PbBr_2$ and transformed $MAPbBr_3$ microwires with 633 nm laser excitation. There are obvious differences in the vibration modes between the $PbBr_2$ microwire and converted $MAPbBr_3$ microwire. The peaks of 29.3 cm^{-1}, 92.5 cm^{-1} and 166.3 cm^{-1} correspond to the terminal Pb-Br stretching frequency (B_{3g}) of $PbBr_6^{4-}$ octahedral in $PbBr_2$ microwires.[1] However, the vibration modes of converted microwire change significantly. Especially, the broad peak of 324.1 cm^{-1} occurs, which is related to MA-cage ($PbBr_6^{4-}$ octahedral) vibration in $MAPbBr_3$.[2] The evolution of low-wavenumber Raman results indicates that the transformed process is complete.

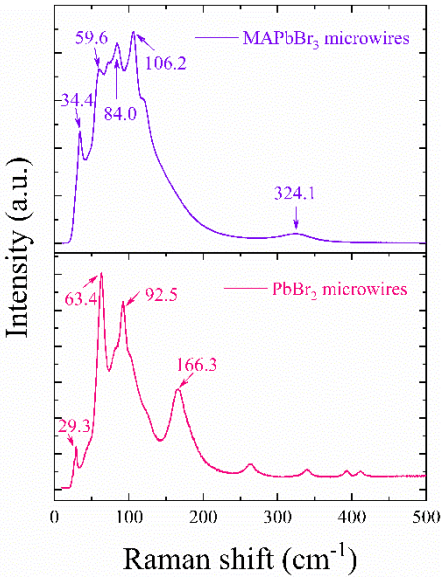

Figure S5. Raman spectra of single $PbBr_2$ microwire and the transformed $MAPbBr_3$ microwire with excitation 633 nm continuous laser.

Figure S6a displays the SEM images of the $FAPbBr_3$ microwires converted from $PbBr_2$ microwires. The smooth surface and no-damage line shape indicates the $FAPbBr_3$ microwires possess high crystal quality after conversion process. Figure S6b shows the EDX mapping of the $FAPbBr_3$ microwires and the C, N, Pb, Br elements are evenly distributed over the mapping area. Moreover, the quantitative elemental analysis infers the Br/Pb ratio is 2.79/1.21, which is in agreement with the stoichiometric ratio of formamidinium lead bromide. Steady-state absorption and PL spectrum of $PbBr_2$ microwires before and after reacted with FABr isopropanol solution were also performed, as shown in Figure S6c. The $PbBr_2$ microwires before conversion shows almost no absorption in entire visible light and no PL emission. In contrast, the sample after conversion behaves obvious absorption edge at 557 nm and strong PL emission with center peak at 543 nm, which is consistent with previous report.[3] Moreover, XRD diffraction results also proves the effectiveness of the conversion process (Figure S6d). The diffraction angle of $PbBr_2$ was almost disappeared after conversion and three new diffraction angles appeared with 14.76°, 29.77° and

45.35°, corresponding to (001), (002) and (003) planes of the cubic phase $FAPbBr_3$, which is consistent with previous report of $FAPbBr_3$ single crystal.[4]

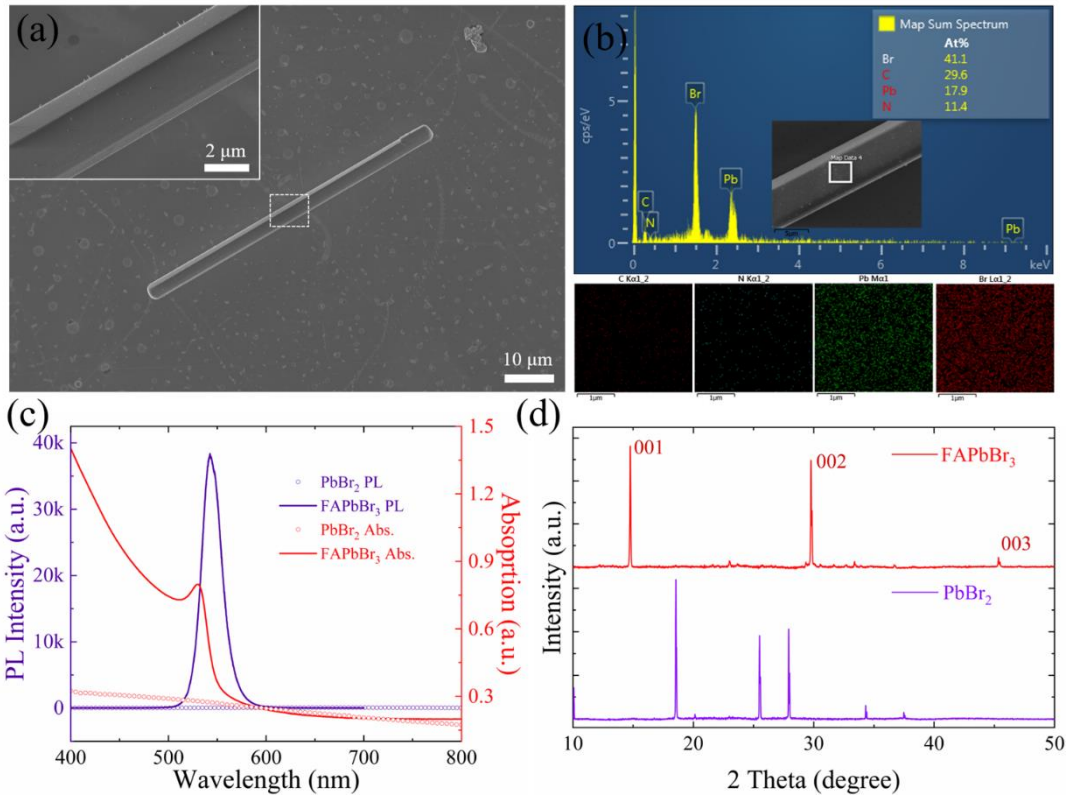

Figure S6. (a) SEM images of the as-converted $FAPbBr_3$ microwires. Inset: the partially enlarged views of the surface. (b)The element of C, N, Pb, Br mapping images from the rectangle area, and the average Br/Pb ratio is 2.79/1.21. (c) Absorption and PL spectrum and (d) XRD patterns of the $PbBr_2$ microwire before and after the conversion process.

Figure S7a shows the temperature dependent PL spectra of single $MAPbBr_3$ microwire with temperature from 80 to 300 K. There is an obvious sharp peak and a weak shoulder toward longer wavelength, which shows common dual emission characteristic in halogen-based perovskite materials. The short wavelength sharp peak emission with center wavelength located at ~542 nm was undoubtedly attributed to direct band edge emission. And the weak transition with the center wavelength at ~548 nm below the direct band edge was attributed to the tail states effects from

indirect transition with static and thermally induced dynamic lattice distortion.[5] When the temperature decreases from room temperature to low temperature 80 K, the PL emission intensity shows a significant increase by two orders of magnitude under 325 nm continuous laser excitation. The phenomenon of PL emission enhancement could only originate from the excitons less affected by thermal dissociation at low temperature. In order to understand the quenching mechanism of the single $MAPbBr_3$ microwire structure, the dependence between integrated PL intensity and temperature was performed as shown in Figure S7b. The PL quenching process shows biexponential decay, hence, the integrated PL emission intensity can be fitted with Arrhenius equation as follows:[6]

$$I(T) = I(0)/[1 + A\exp(-E_b/k_BT)]$$

Where *I(0)* represent the integrated PL intensities at temperature at 0 K. A is the constant of thermal quenching process, k_B is the Boltzmann constant. E_b is the exciton binding energy. The fitting (red line) results derive the exciton binding energy E_b = 75 meV. The exciton binding energy of 75 meV is very close to the value of 76 meV bulk $MAPbBr_3$ single crystal in the previous report,[7, 8] Hence, the high bound exciton energy close to bulk single crystal ensures the stability for laser emission at room temperature (k_BT = 26 eV at 300 K).

Figure S7c shows the temperature-dependent PL emission wavelength and derived optical bandgap of $MAPbBr_3$ microwire. Interestingly, the bandgap shows a trending rise (blue shift) with the increasing temperature. The phenomenon of blue shift is different from previous generation semiconductors, such as ZnO, InP, Si, whose bandgap usually redshift with the increasing temperature. In addition, the blue shift is a common phenomenon in lead composite perovskite and the possible reasons could be attributed to the reverse ordering of the band edge[9] and the interplay between the electron-phonon renormalization[10]. The continuous rise of band gap could be depicted

by a thermal coefficient κ, which simultaneously affected by two mechanism of lattice thermal expansion and electron-phonon expansion.[10] In general, the influence of thermal expansion coefficient on the compact lattice structure of traditional semiconductors is so small that it could be ignored. However, the lead composite perovskite needs to consider the impact of the two mechanisms at the same time. According to the previous reports, the continuous broadening of optical bandgap can be approximately described by the relation $\kappa = \partial E/\partial T$.[11] There are three different bandgap increase regions in the fitting results, which can be attributed to the phase change of $MAPbBr_3$ with different temperature. The thermal coefficients of bandgap distributed as κ_1 = 0.226 meV/K (T<150 K), κ_2 = 0.181 meV/K (150 K<T<220 K), κ_3 = 0.088 meV/K (T>220 K), which corresponds to orthorhombic phase, tetragonal phase, cubic phase, respectively.[2] Thus, the phase change temperature transition point of the $MAPbBr_3$ microwire is about 150 and 220 K.

To further demonstrate the exciton-phonon coupling in $MAPbBr_3$ microwire, a detailed analysis of the temperature dependent fwhm of the center emission wavelength is shown in Figure S7d. The fwhm of the PL emissions increases with the increasing of temperature, implying the broadening of the PL peaks, which can be described by the independent Boson model:[8]

$$\Gamma(T) = \Gamma_0 + \beta T + \Gamma_{LO}/[\exp(\hbar\omega_{LO}/k_B T) - 1]$$

where Γ_0 is the inhomogeneous broadening parameter, β is excitonic longitudinal acoustic phonon factor, Γ_{LO} is excitonic longitudinal optical phonon contribution factor and $\hbar\omega_{LO}$ is the optical phonon energy. At low temperature, the fwhm can be considered to the dominant inhomogeneous broadening of inactive phonons.[12] The optical phonon energy $\hbar\omega_{LO}$ was calculated as ~39.2 meV from the fitting results, indicating strong exciton-optical phonon coupling interactions. Simultaneously, the obtained optical energy is consistent with the above Raman vibration energy in

the ~325 cm^{-1} position, which is assigned to the MA-$PbBr_3$ cage vibrations.

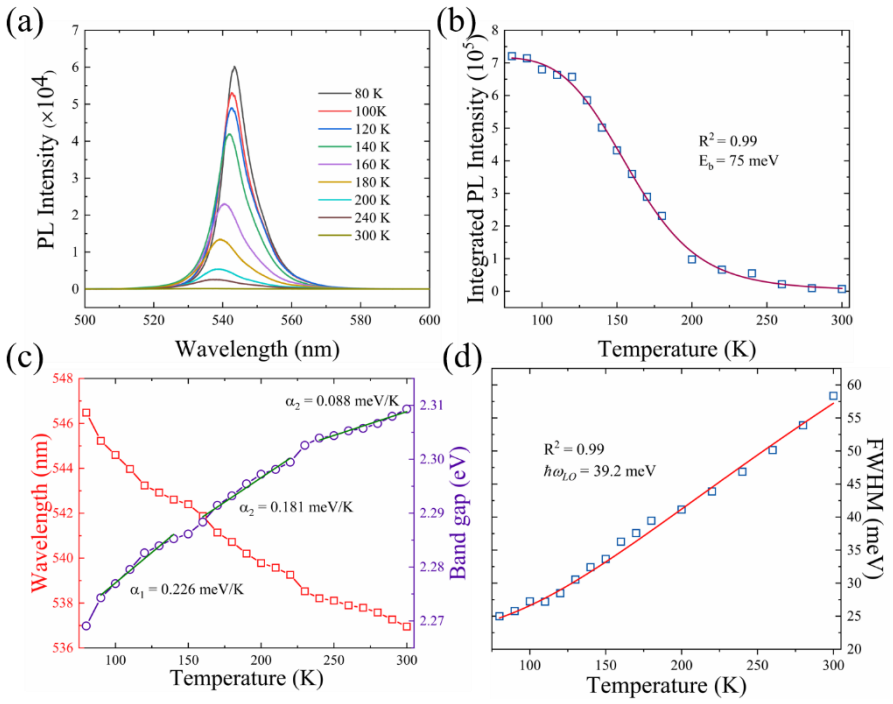

Figure S7. (a) The temperature-dependent PL emission spectra of single microwire; (b)The integrated PL intensity as a function of temperature. (c) The emission peak wavelength of $MAPbBr_3$ microwire and the calculated bandgap as a function of temperature. (d) Plots of the emission peak fwhm with the increase of temperature.

The $FAPbBr_3$ microwires obtained following the similar synthesis route can also support the lasing action, as shown in Figure S8. The SEM image of the single $FAPbBr_3$ microwire with the length ~55 μm was displayed in Figure S8a. With the increasing pump density, the PL spectra also transited from SE to ASE. Six modes lased simultaneously when the pump density reached the threshold, as shown in the inset of Figure S8b. The FWHM of the emission center wavelength at 553 nm is about 0.23 nm, and the corresponding Q factor can be calculated as 2404, which is higher than the previous reports.[13] Figure S8c showed the log-log plot of integrated emission intensity versus pump density, exhibiting a clear "S" shape. The first turning point represents the lasing threshold and the value is 19.9 μJ/cm^2, which is lower than that of $MAPbBr_3$ microlaser. The inset

of Figure S6c shows the fluorescent microscopy images below and above lasing threshold, respectively. The bright spots at the two ends implies the built-in microlaser behaves the FP mode properties. As a result, the realization of the $FAPbBr_3$ microlaser proves that the synthesized sample possesses high crystal quality, and it also shows the general adaptability of our synthesis method.

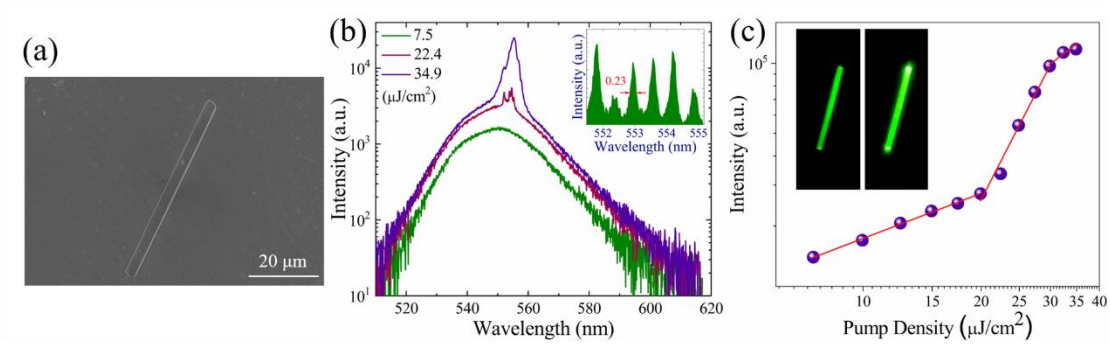

Figure S8. (a) Top view SEM image of the individual $FAPbBr_3$ microwire. (b) Pump dependent emission spectra of the $FAPbBr_3$ microwire; Inset: high-resolution laser spectrum around threshold. (c) The integrated emission intensity as a function of pump density. Insets: the fluorescent microscopy images of the microwire below and above threshold.

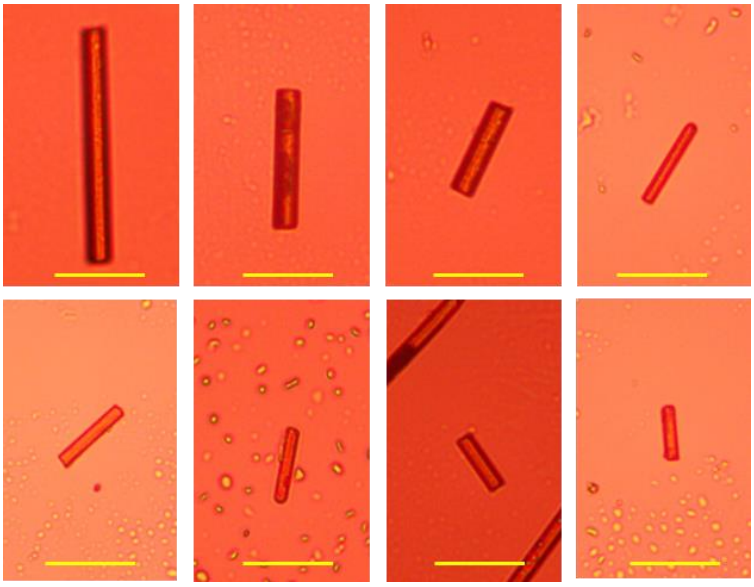

Figure S9. The optical microscopy images of the $MAPbBr_3$ microwires with different length collected by transmitted light, which were used for mode control lasing. Scale bar: 20 μm.

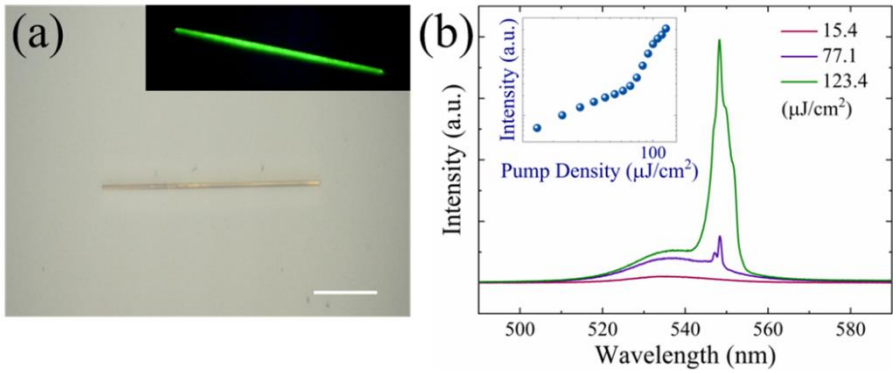

Figure S10. (a) Optical microscopy image of an ultralong $MAPbBr_3$ microwire with length of about 343.5um; the inset shows fluorescent microscopy image of the microwire laser, scale bar: 100 μm. (b) Power density dependent emission spectra of the microwire; Inset: the integrated emission intensity as a function of pump density. Clear threshold behavior can be observed. The diameter of the pump spot size is adjusted to 400 μm and the ultralong microwire was fully covered with the spot.

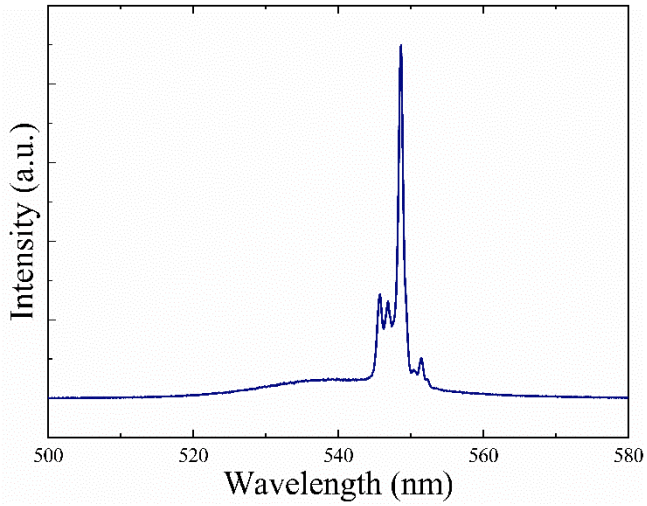

Figure S11. The laser emission spectra of single $MAPbBr_3$ microwire under constant pulsed excitation power (1.2 P_{th}) in N_2 atmosphere.

References

(1) Plekhanov, V. G. Lead Halides: Electronic Properties and Applications. *Prog. Mater. Sci.* **2004**, *49*, 787-886.

(2) Wang, K. H.; Li, L. C.; Shellaiah, M.; Sun, K. W. Structural and Photophysical Properties of Methylammonium Lead Tribromide ($MAPbBr_3$) Single Crystals. *Sci Rep* **2017**, *7*, 1-14.

(3) Chen, S.; Nurmikko, A. Stable Green Perovskite Vertical-Cavity Surface-Emitting Lasers on Rigid and Flexible Substrates. *Acs Photonics* **2017**, *4*, 2486-2494.

(4) Zhumekenov, A. A.; Saidaminov, M. I.; Haque, M. A.; Alarousu, E.; Sarmah, S. P.; Murali, B.; Dursun, I.; Miao, X.-H.; Abdelhady, A. L.; Wu, T. Formamidinium Lead Halide Perovskite Crystals with Unprecedented Long Carrier Dynamics and Diffusion Length. *ACS Energy Lett.* **2016**, *1*, 32-37.

(5) Wu, B.; Yuan, H.; Xu, Q.; Steele, J. A.; Giovanni, D.; Puech, P.; Fu, J.; Ng, Y. F.; Jamaludin, N. F.; Solanki, A. Indirect Tail States Formation by Thermal-Induced Polar Fluctuations in Halide Perovskites. *Nat. Commun.* **2019**, *10*, 1-10.

(6) Xing, G.; Luo, J.; Li, H.; Wu, B.; Liu, X.; Huan, C. H. A.; Fan, H. J.; Sum, T. C. Ultrafast Exciton Dynamics and Two□Photon Pumped Lasing from ZnSe Nanowires. *Adv. Opt. Mater.* **2013**, *1*, 319-326.

(7) Tanaka, K.; Takahashi, T.; Ban, T.; Kondo, T.; Uchida, K.; Miura, N. Comparative Study on The Excitons in Lead-Halide-Based Perovskite-Type Crystals $CH_3NH_3PbBr_3$ $CH_3NH_3PbI_3$. *Solid State Commun.* **2003**, *127*, 619-623.

(8) Zhang, F.; Zhong, H.; Chen, C.; Wu, X.-g.; Hu, X.; Huang, H.; Han, J.; Zou, B.; Dong, Y. Brightly Luminescent and Color-Tunable Colloidal $CH_3NH_3PbX_3$ (X= Br, I, Cl) Quantum Dots: Potential Alternatives for Display Technology. *ACS Nano* **2015**, *9*, 4533-4542.

(9) Milot, R. L.; Eperon, G. E.; Snaith, H. J.; Johnston, M. B.; Herz, L. M. Temperature□Dependent Charge□Carrier Dynamics in $CH_3NH_3PbI_3$ Perovskite Thin Films. *Adv. Funct. Mater.* **2015**, *25*, 6218-6227.

(10) Wu, K.; Bera, A.; Ma, C.; Du, Y.; Yang, Y.; Li, L.; Wu, T. Temperature-Dependent Excitonic Photoluminescence of Hybrid Organometal Halide Perovskite Films. *Phys. Chem. Chem. Phys.* **2014**, *16*, 22476-22481.

(11) Dai, J.; Zheng, H.; Zhu, C.; Lu, J.; Xu, C. Comparative Investigation on Temperature-Dependent Photoluminescence of $CH_3NH_3PbBr_3$ and $CH(NH_2)_2PbBr_3$ Microstructures. *J. Mater. Chem. C* **2016**, *4*, 4408-4413.

(12) Li, X.; Wang, K.; Chen, M.; Wang, S.; Fan, Y.; Liang, T.; Song, Q.; Xing, G.; Tang, Z. Stable Whispering Gallery Mode Lasing from Solution□Processed Formamidinium Lead Bromide Perovskite Microdisks. *Adv. Opt. Mater.* **2020**, *8*, 2000030.

(13) Fu, Y.; Zhu, H.; Schrader, A. W.; Liang, D.; Ding, Q.; Joshi, P.; Hwang, L.; Zhu, X.; Jin, S. Nanowire Lasers of Formamidinium Lead Halide Perovskites And Their Stabilized Alloys With Improved Stability. *Nano Lett.* **2016**, *16*, 1000-1008.